CrossMark

METHODS

An Integrated Force Probe and Quartz Crystal Microbalance for High-Speed Microtribology

Brian P. Borovsky[1] · Christopher Bouxsein[1] · Cullen O'Neill[1] · Lucas R. Sletten[1]

Abstract We have developed a technique for measuring frictional forces and contact areas, over a wide range of applied loads, at microscopic contacts reaching high sliding speeds near 1 m/s. Our approach is based on integrating two stand-alone methods: nanoindentation and quartz crystal microbalance (QCM). Energy dissipation and lateral contact stiffness are monitored by a transverse shear quartz resonator, while a spherical indenter probe is loaded onto its surface. Variations in these two quantities as functions of shear amplitude, with the normal load held fixed, reveal a transition from partial to full slip at a critical amplitude. Average values of both the threshold force for full slip and the kinetic friction during sliding are determined from these trends, and the contact area is inferred from the lateral stiffness at low shear amplitudes. Measurements are performed at loads ranging from 5 μN to 8 mN using an electrostatically actuated indenter probe. For the materials chosen in this study, we find that the full slip threshold force is about a factor of two larger than kinetic friction. The forces increase sublinearly with load in close correspondence with the contact area, and the shear strengths are found to be relatively insensitive to pressure. The threshold shear amplitude scales in proportion to the contact radius. These results demonstrate that the probe–QCM technique is a versatile and full-featured platform for microtribology in the speed range relevant to practical applications.

1 Introduction

Efforts to develop mechanical devices at micrometer length scales have required designs that either avoid contact between moving parts or employ novel techniques to manage constraints imposed by the basic tribological phenomena of adhesion, friction, and wear [1–4]. These challenges highlight the need for an improved understanding of microtribology, the regime where interfaces contain just a few asperities in close contact [5, 6]. Scanning probe studies of nanoscale single-asperity contacts have brought a wealth of new insights into fundamental processes; however, the sliding speeds achieved are typically far slower than encountered in practical devices [4, 6–8]. Traditional pin-on-disk tribometers can investigate realistic multi-asperity contacts at device-relevant speeds from 100 mm/s to 1 m/s, but these instruments are intended for macroscopic interfaces containing perhaps millions of asperities. There remains a need for new experimental approaches that bridge the gaps between nanoscopic and macroscopic methods to develop a multiscale understanding of interfaces and open new avenues for engineering applications such as microelectromechanical systems, hard disk drives, and precision medical devices [5, 6]. In this paper, we report on a microtribometer formed by integrating two instruments, a nanoindentation probe and a quartz crystal microbalance (QCM). We show that our technique is capable of studying the frictional properties of microscopic contacts at high sliding speeds over a wide range of applied loads.

✉ Brian P. Borovsky
   borovsky@stolaf.edu

[1] Department of Physics, St. Olaf College, 1520 St. Olaf Ave, Northfield, MN 55057, USA

The precisely defined resonances of thin quartz disks led to their earliest applications as stable time bases in electronic circuits and thickness monitors in film deposition systems [9, 10]. Today, the quartz crystal microbalance is used as a sensitive probe of surface interactions in a wide variety of scientific contexts [11, 12]. The use of QCM for fundamental studies of friction was initiated in the late 1980s by Krim et al. [13–15], in a series of experiments on the sliding of noble gas monolayers adsorbed onto metallic surfaces at cryogenic temperatures. Around this time, Dybwad [16] studied the elastic and inertial effects of attaching small spheres to the QCM surface. These experiments inspired a variety of studies employing sharp tips or spheres in contact with QCMs to measure local elastic and dissipative properties, the mechanics of small contacts, and friction-induced melting [17–26]. The 'probe–QCM' technique was further developed in experiments where the state of relative motion at the interface could be unambiguously determined, whether stuck, partially slipping, or in full slip at high sliding speeds [27–29]. The most recent studies have carefully explored the transitions between these states of motion as the QCM shear amplitude is increased, leading to measurements of the associated lateral stiffnesses, elastic and dissipative forces, contact areas, and shear strengths [30–35]. This has included observations at the nanoscale using atomic force microscope tips [34, 35].

These results highlight the avenues for conducting quantitative micro/nanotribology with the probe–QCM approach. However, the prior experiments with contacts in full slip conditions were carried out at a single applied load or narrow range of loads. Here we perform measurements over an extended load range in order to provide a more complete analysis of tribological phenomena, closer to that routinely achieved in more established probe-based methods. This includes investigating the variation in frictional forces and contact areas with load and evaluating the extent to which the observed shear strengths depend on externally applied pressure. In addition, we find that the threshold force to initiate full slip is significantly larger than the average kinetic friction. Meanwhile, the shear amplitude required for sliding increases with the radius of contact. We address the implication of our results for theories of microslip.

2 Methods

2.1 Operating Principles and Overview of Equipment

The principles of operation of our probe–QCM tribometer are as follows. A force probe loads a spherical tip onto the surface of a quartz crystal microbalance (QCM), as depicted in Fig. 1a. The QCM surface oscillates laterally at frequencies in the MHz range. The amplitude of the
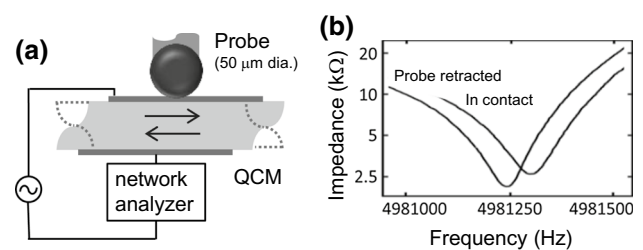
Fig. 1 a A diagram of the integrated probe–quartz crystal microbalance (QCM) tribometer. The crystal used in the present study had a nominal fundamental frequency of 5 MHz. **b** Contact between the tip and surface alters the quartz crystal's resonance curve. These observations allow the elastic and dissipative forces acting at the interface to be quantified

lateral motion depends on the drive level, but can commonly reach values near 50 nm. This results in maximum surface speeds over 1 m/s. It is important to emphasize that the resonating quartz crystal not only provides the shearing motion responsible for interfacial slip, but also senses the lateral forces acting at the interface.

The probe tips may be chosen from any material and generally range in diameter from micrometers to millimeters. The QCM is an AT-cut quartz crystal in the shape of a thin circular disk about 1 cm in diameter with metallic electrodes on its top and bottom surfaces. These sensors are commercially available with a wide variety of electrode materials and coatings. The electrode surfaces may be modified as desired by depositing overlayers and lubricant films, or by attaching atomically flat surfaces such as mica or graphite that can be freshly cleaved before testing [34–37].

The QCM is driven electrically at frequencies corresponding to resonances of the crystal. AT-cut quartz crystals resonate in transverse thickness shear mode, causing laterally directed sinusoidal motion at the surfaces. In the present study, we employed only the 5-MHz fundamental mode. A network analyzer (Agilent/Keysight, E5100A with options 618, 41900A, and 1D5) is used to evaluate the resonance properties [21]. The analyzer performs frequency sweeps, while measuring the electrical impedance of the system. The impedance reaches a minimum value at the resonance condition corresponding to peak motion of the crystal, as shown in Fig. 1b. Each resonance curve is fit to the Butterworth–van Dyke equivalent circuit model to determine the series resonant frequency f_{res}, inductance L, and resistance R of the crystal [21, 32]. The quality factor is $Q = 2\pi f_{res}/(R/L)$, where (R/L) is the full bandwidth of the resonance. The values of Q during the present experiments remained above 60,000.

The force probe employed is an electrostatically actuated nanoindenter capable of applying a range of loads from about 1 μN to 10 mN (Hysitron, TriboScope® one-dimensional

transducer). The QCM is mounted in its holder onto an XYZ piezo scanner base (Veeco/Bruker, NanoScope II®).

2.2 Physical Quantities Measured by the QCM

When the spherical tip is loaded onto the QCM surface, the resulting lateral forces acting at the interface alter the resonance properties of the crystal. A typical example is shown in Fig. 1b. The frequency and bandwidth of the resonance both increase due to tip-surface contact. The upward shifts in these resonance parameters are quantified by Δf_{res} and ΔQ^{-1}. These values determine two distinct physical properties of the interface: the effective lateral stiffness,

$$k = 4\pi (MK)^{1/2} \Delta f_{\text{res}} \tag{1}$$

and the additional energy dissipated per cycle due to tip-surface contact,

$$\Delta W_{\text{loss}} = \pi K U_0^2 \Delta Q^{-1} \tag{2}$$

where $M = 5.0\,\text{mg}$ and $K = M(2\pi f_{\text{res}})^2$ are the effective mass and stiffness of the quartz disk, respectively [29, 32], and U_0 is the peak lateral oscillation amplitude near the center of the disk. The effective mass is computed from the density of quartz, the thickness of the disk, and the active area of the electrode: $M = \frac{1}{2}\rho A_e h$, where the factor of $\frac{1}{2}$ accounts for the variation in shear amplitude throughout the thickness of the disk. It is important to note that the interaction forces between the tip and surface are closely confined to the interface due to the 'near-field' acoustic geometry of the setup: The wavelength of 5-MHz shear waves in quartz is over 600 μm, much larger than the contact radii obtained, near 1 μm [21]. Also, the duration of each resonance measurement is several seconds, whereas the crystal undergoes millions of oscillations each second. Therefore, the measured parameters k and ΔW_{loss} represent values averaged over millions of cycles.

The lateral contact stiffness k is converted to the amplitude of the effective elastic force using the relation:

$$F_s = k U_0 \tag{3}$$

In Sect. 3 below, we show that plots of F_s and ΔW_{loss} versus amplitude U_0 facilitate an understanding of relative motion at the interface. From this analysis, two characteristic forces are determined: the threshold force to enter the full slip state, denoted by F_s^*, and the kinetic friction F_k. In addition, the low-amplitude limit of k provides an assessment of the contact size. It is clear that the interactions observed in the present work are nonlinear because the stiffness k depends on oscillation amplitude. In Sect. 3.3, we discuss the instantaneous forces acting at the interface and justify the use of the linear viscoelastic relations above with reference to a recent perturbation theory analysis by Hanke et al. [32].

We note that Eq. (1) is derived from a first-order expansion of the resonant frequency of a lightly damped harmonic oscillator:

$$f_{\text{res}} \simeq \frac{1}{2\pi} \sqrt{\frac{K + k}{M}} \tag{4}$$

and Eq. (2) is a rearrangement of the relationship:

$$\Delta Q^{-1} = \Delta \left(\frac{W_{\text{loss}}}{2\pi E} \right) \tag{5}$$

where the mechanical energy stored in the oscillator is given by $E = \frac{1}{2} K U_0^2$. The oscillation amplitude is computed from the empirical formula:

$$U_0 = (1.4\,\text{pm/V}) \cdot Q \cdot V_p \tag{6}$$

where Q is measured as described above, and V_p is the peak amplitude of the sinusoidal drive voltage across the crystal's electrodes at resonance, measured with a digital oscilloscope (Tektronix, TDS 2002B) [38]. There is a measurement uncertainty of 7% in the prefactor of 1.4 pm/V, which is a source of systematic error in the amplitude U_0. Meanwhile, the random error in U_0 is dominated by fluctuations of about 5% in the voltage V_p. The range of amplitudes accessed in the present study spanned from 1 to 70 nm, using a 5-MHz crystal. Therefore, the maximum surface speeds at the midpoint of the crystal's reciprocating motion ranged from 0.03 to 2.2 m/s, as inferred from the relation $v = U_0 \cdot 2\pi f_{\text{res}}$. Equation (6) was determined in a previous experiment using scanning tunneling microscope images of a QCM vibrating in its 5-MHz fundamental resonance mode [38]. Alternatively, the amplitude can be related to the nominal output voltage of the network analyzer, the piezoelectric stress coefficient of quartz, and geometric properties of the selected quartz disk [32, 39]. This approach has been found to be in good agreement with the empirical formula used here [39].

2.3 Testing Protocol

Each trial consists of amplitude-dependent measurements of Δf_{res} and ΔQ^{-1}. We observe that driving the QCM at high shear amplitudes with the tip engaged helps to run in the interface and establish reproducible signals, as others have reported [29]. The shifts Δf_{res} and ΔQ^{-1} are computed over the available amplitude range by comparing the values measured with and without the tip engaged. In the present study, two of the 100-μN trials and the 5-μN trials were conducted with the selected QCM amplitudes accessed in random order. The results were comparable to those obtained using linear amplitude ramps.
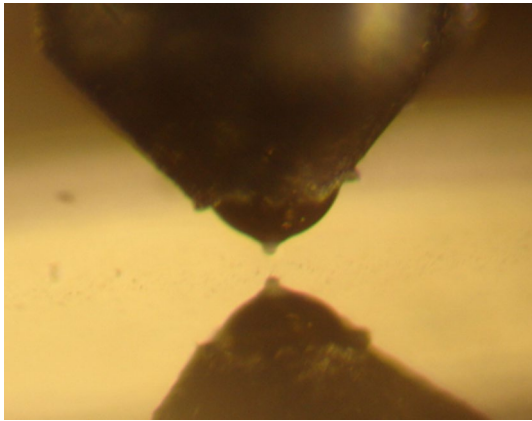
Fig. 2 Photograph of the microsphere probe and its reflection in the optically flat gold electrode on the top surface of the QCM. Visible are the tapered end of the probe shaft, the sapphire ball capping the hole down the center of the shaft, and the aluminum oxide microsphere attached with epoxy. The diameter of the microsphere is 50 μm. The electrode has a monolayer of octadecanethiol deposited onto its surface

2.4 Materials

The following materials were selected for the present study in order to demonstrate the technique. The substrate was an AT-cut quartz crystal with a nominal resonant frequency of 5 MHz, optically polished surfaces, and 100-nm-thick gold electrodes with rms roughness values near 10 nm (ICM, Inc). A monolayer of octadecanethiol (C18) was chemisorbed from ethanol solution onto the electrode surfaces. The probe tip was a 50-μm-diameter sphere of polycrystalline α-Al$_2$O$_3$ with a typical grain size of 5 μm (microspheresnanospheres.com). The effects on our results of the grain size, roughness, or other properties of these microspheres as fabricated are unknown, although plastic deformation of the softer gold substrate and interfacial wear are expected. The probe and quartz crystal were cleaned by rinsing in ethanol and DI water and drying in a nitrogen flow. The measurements were performed in ambient conditions with RH ~ 40%.

The microsphere probe was assembled using a technique developed in house, similar to the approach described in Mak et al. [40]. Starting with a standard tip holder from Hysitron, Inc., the hole down the center of the shaft was filled with a two-component epoxy (Loctite, Hysol® 1C) and capped with a sapphire ball whose diameter was 0.5 mm (0.0197", smallparts.com). The microsphere was glued to the apex of this ball using a small drop of the same epoxy. Both the epoxy drop and the sphere were handled using pulled glass pipettes attached to a micromanipulator under a long working distance binocular microscope. A photograph of the assembled probe is shown in Fig. 2.

3 Results and Discussion

3.1 Lateral Contact Stiffness: A Transition from Partial to Full Slip

The behavior of the lateral contact stiffness with increasing QCM amplitude is shown in Fig. 3a for a representative data set acquired at an applied load of 1 mN. We observe a trend of weakening stiffness as the shear amplitude grows. This type of nonlinear elastic response signals the occurrence of interfacial microslip and has been reported in a number of probe–QCM studies [27–35]. Microslip is expected on general grounds for sphere-plane contacts within the theories of Cattaneo and Mindlin (CM) [41–43] and Savkoor [43, 44]. These theories conclude that the interface obtains its highest stiffness as the shear amplitude approaches zero because the entire contact region remains stuck during the cyclical motion. Increasing the amplitude causes an annulus of slip to initiate on the outer periphery of the contact, and this partial slip lowers the effective stiffness of the contact. The size of the slip zone continually increases with oscillation amplitude because the inner boundary of the slip annulus moves further inward. At a critical amplitude, the stuck central portion of the contact is eliminated, marking the transition from partial to full slip.

3.2 Elastic Forces and the Threshold of 'Static' Friction

Direct evidence of the transition to full slip is shown in Fig. 3b. Here we compute the amplitude of the oscillatory elastic force using $F_s = k U_0$. We find that F_s increases in a sublinear fashion with U_0 and reaches a plateau F_s^* at a critical amplitude U_0^*. For this trial with a load of 1 mN, the plateau value is $F_s^* = 2.04 \pm 0.05$ mN. When the amplitude is less than U_0^*, we find good agreement with the CM microslip relation for the size of the tangential force at the endpoints of the oscillation: $F_s = F_s^* (1 - (1 - U_0/U_0^*)^{3/2})$ [41, 42]. The Savkoor theory derives a nearly identical curve with a more complicated mathematical form [33, 44, 45]. The plateau in our observed elastic force provides empirical evidence that the contact enters a full slip state. This interpretation is supported by the CM and Savkoor models, for which the onset of full slip corresponds to a maximum in the tangential restoring force. We identify F_s^* with the threshold force of static friction, since it is in phase with the displacement, although recognizing this occurs at MHz frequencies.

3.3 Kinetic Friction in Full Slip

We now determine the kinetic friction during full slip using measurements of the dissipated energy and its dependence on the amplitude of motion. Figure 3c displays
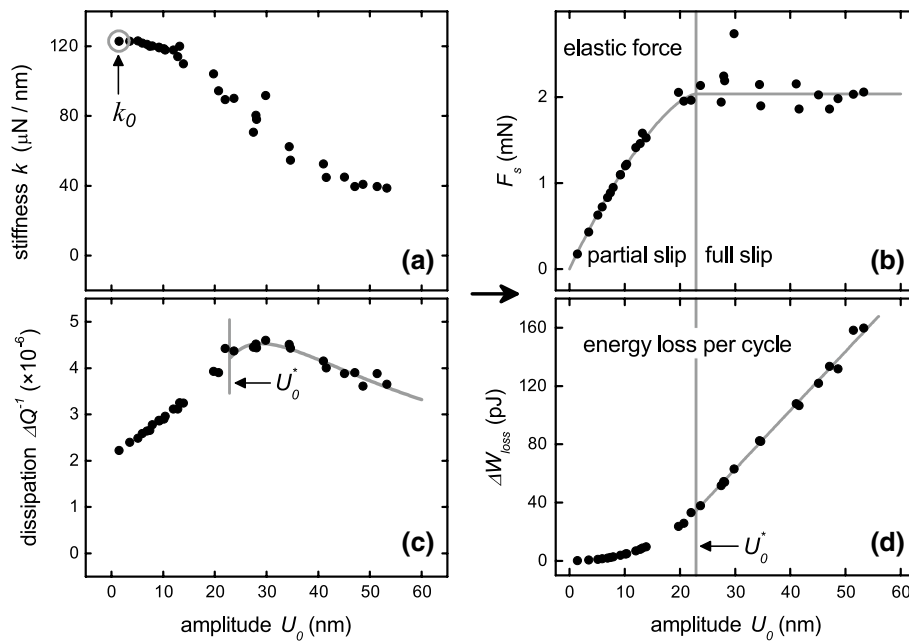
Fig. 3 Lateral stiffness (**a**) and elastic force (**b**) versus shear amplitude. The initial weakening of the stiffness with amplitude signals partial slip within the contact zone. The elastic force rises to a plateau value that indicates the threshold required to initiate full slip. Vertical gray lines mark the critical amplitude separating the partial and full slip regimes. In (**b**), the Cattaneo–Mindlin model is plotted as a solid curve in the partial slip regime. Dissipation factor (**c**) and normalized energy loss per cycle (**d**) versus shear amplitude. The linear increase in energy dissipated in the full slip regime, indicated by the solid line in (**d**), provides a direct measurement of the average kinetic friction. In (**c**), the function corresponding to the linear trend in (**d**) is shown as a solid curve

the trend in ΔQ^{-1} versus amplitude U_0. Figure 3d displays the resulting variation in the interfacial energy loss per cycle, as computed from Eq. 2 using the observed values of ΔQ^{-1}. We find that ΔW_{loss} increases linearly with amplitude in the full slip range, $U_0 > U_0^*$. The simplest interpretation is that this trend represents the work done each cycle by a constant average frictional force F_k acting over increasingly large distances as the amplitude of the cyclic motion is increased.

To illustrate this idea, two instantaneous force–distance loops for a reciprocating interface are shown in Fig. 4. Both loops feature constant forces during full slip and curved portions associated with partial slip. The area enclosed by each loop is the work done by friction, equating to the energy dissipated per cycle. In both cases, the energy loss grows linearly as the displacement amplitude increases as long as the full slip forces remain constant. Note that the values on the horizontal axis are in units of U_0^*, the amplitude at which full slip begins to occur. These force loops are speculative. It is not possible to reconstruct the complete details of the instantaneous loops using only the two values measured for a given amplitude of motion via the QCM frequency and quality factor shifts. However, one can propose any loop shape and compute the expected resonance shifts using perturbation theory, a topic that

has been thoroughly developed by Hanke et al. [32]. Two significant findings of this analysis are as follows: Firstly, the effective elastic force obtained from Eqs. (1) and (3) represents a weighted average over the entire loop that is
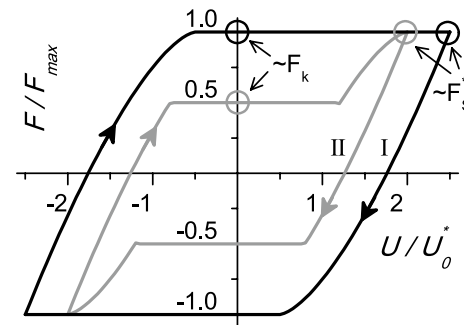
Fig. 4 Instantaneous force–distance hysteresis loops. Each loop represents a way to realize linear growth in energy loss (enclosed area) with increasing oscillation amplitude. The horizontal flats represent the constant value of kinetic friction in full slip for each loop. The curved sloped portions reflect the lateral force during partial slip and are derived from the Cattaneo–Mindlin model. The contact becomes stuck at the endpoints of the motion, where the velocity reaches zero, then undergoes a transition from partial to full slip. In loop I, the maximum elastic force at the endpoints is equal to the full slip kinetic friction. In loop II, kinetic friction is smaller by a factor of two, a difference that corresponds to our experimental results

most influenced by the instantaneous forces near the end-points of the motion; secondly, the frictional energy loss represented by the enclosed area relates to the change in quality factor in exactly the same way as for a viscously damped harmonic oscillator. The latter finding justifies the use of Eq. (2) with the understanding that ΔW_{loss} is rigorously equal to the energy loss per cycle regardless of the specific force law.

Aided by this discussion of force loops, we now complete our analysis of the linear trend in ΔW_{loss} versus U_0 shown in Fig. 3d. The distance traveled in the full slip state during each complete cycle is given by $4(U_0 - U_0^*)$. We account for the total cyclic energy loss with the equation $\Delta W_{\text{loss}} = F_k \cdot 4(U_0 - U_0^*) + \Delta W_{\text{loss}}^*$, where ΔW_{loss}^* is the energy loss (enclosed area) observed at the threshold amplitude $U_0 = U_0^*$. A linear fit to this equation for $U_0 > U_0^*$ yields the value of F_k. We find a kinetic friction of $F_k = 1.01 \pm 0.02$ mN for the data in Fig. 3d.

In Fig. 3c, we display the corresponding fit curve for ΔQ^{-1} versus U_0, obtained from Eq. (2) by substituting our linear model for the energy loss:

$$\Delta Q^{-1} = \frac{\Delta W_{\text{loss}}}{\pi K U_0^2} = \frac{1}{\pi K}\left[\frac{4F_k}{U_0} + \frac{(\Delta W_{\text{loss}}^* - 4F_k U_0^*)}{U_0^2}\right] \quad (7)$$

It is interesting that for the data set in Fig. 3c, the curve describing ΔQ^{-1} reaches its peak at an amplitude larger than $U_0 = U_0^*$. In general, the peak in ΔQ^{-1} can occur at an amplitude less than, equal to, or greater than U_0^* depending on the values of ΔW_{loss}^*, F_k and U_0^*. A more reliable indication of the threshold for full slip is given by the amplitude at which the elastic force reaches a maximum, as in Fig. 3b, or where the energy loss grows linearly, as in Fig. 3d.

To summarize our results for the 1-mN trial, the observed kinetic friction of $F_k = 1.01 \pm 0.02$ mN is a factor of two smaller than the static friction limit of $F_s^* = 2.04 \pm 0.05$ mN. Kinetic friction is generally expected to be smaller than static friction, and differences of this size are common for macroscopic systems. However, such an effect has not been previously reported from probe–QCM measurements. Linear increases in energy dissipation with amplitude were observed in three previous studies [30, 34, 35]. In one case, a comparison was made between the measured elastic and dissipative forces. The kinetic friction was judged to be roughly equal to the threshold for full slip [30]. The authors concluded that their results are consistent with loop I in Fig. 4, where $F_k \sim F_s^*$. In contrast, our results are consistent with a cycle such as loop II, where $F_k \sim \frac{1}{2}F_s^*$. However, these loops are merely simple cases consistent with the respective experimental findings. Other loop shapes are possible that are

broadly similar to these but differing in details, and these may be more physically reasonable. For example, variations about the constant kinetic friction values shown may leave the predicted dissipation signals unchanged, as long as the total enclosed area of the loop is preserved. Also, the predicted elastic force F_s is relatively unaffected by the forces that occur during the middle of the motion away from the extreme endpoints [32].

Our analysis of the data in terms of elastic forces and energy dissipation has assumed that the relative motion at the interface is entirely tangential. While the observed trends with increasing shear amplitude fit this model well, we cannot rule out the possibility of contributions from motions normal to the interface due to flexural modes of the quartz crystal. These modes are understood to contribute to the oscillation of thickness shear crystals, particularly at the fundamental frequency [46].

We now provide illustrative comparisons to results in the literature to complement the interpretation presented here. These studies demonstrate that contrasting physical behaviors at the interface produce correspondingly different amplitude-dependent trends in the measured quantities. For example, in three recent probe–QCM studies linear viscoelastic responses were observed over the entire available range of shear amplitudes [29, 30, 32]. This occurred when polymer films at the interface were sufficiently thick [29, 30], or when the spherical probes were relatively small [32]. Apparently the shear stresses in either case were not large enough to cause partial slip, and the dissipation reflected the internal damping of stuck contacts. In contrast to the linear growth in ΔW_{loss} during full slip reported here, viscous damping produces quadratic increases with amplitude. This is due to the fact that the maximum QCM surface velocity increases with amplitude, through $v_{\text{max}} = 2\pi f_{\text{res}} \cdot U_0$. Thus, the maximum drag force, attained at the midpoint of each cycle, is proportion to the amplitude, and the area enclosed by the force–distance loop increases with amplitude squared. Another example regards friction-induced melting. In one recent probe–QCM study, melting at the interface between a tip and indium surface was observed through the detection of negative, rather than positive, shifts in the QCM resonant frequency [25].

3.4 Contact Area Measurements Using the Lateral Stiffness

The understanding of tribological systems can be greatly enhanced by separately assessing how the measured frictional forces depend on applied load and contact area. To this end, we infer the contact area A directly from the low-amplitude lateral stiffness using the approach developed in Leopoldes et al. [29, 47, 48]. An important advantage
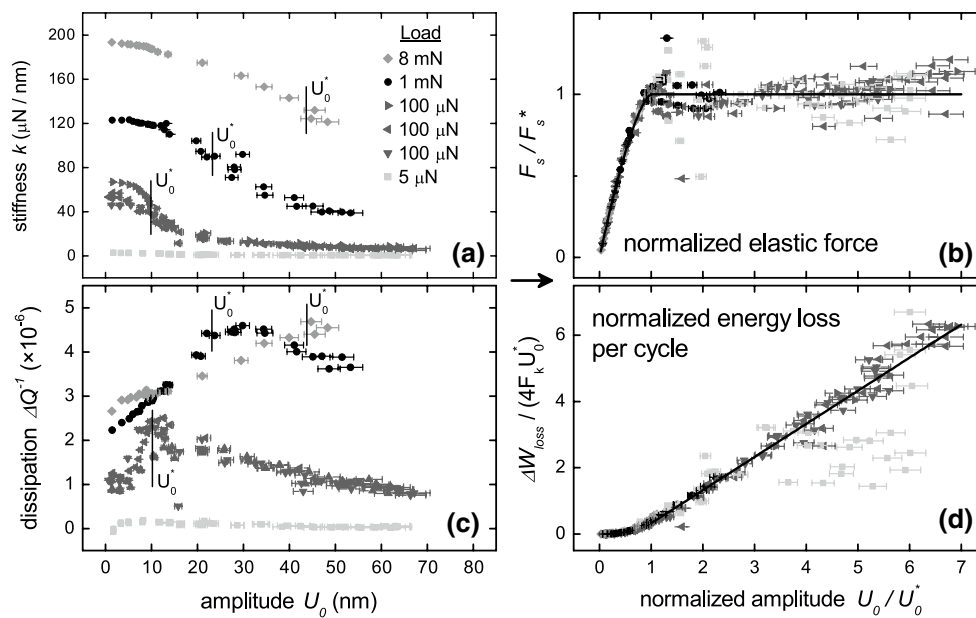
Fig. 5 Lateral stiffness (**a**), normalized elastic force (**b**), dissipation factor (**c**), and normalized energy loss per cycle (**d**) versus shear amplitude, for a range of applied normal loads. The data sets in (**a**) and (**c**) are seen to collapse to common curves in (**b**) and (**d**), respectively. This is achieved by normalizing the y-axis values using the characteristic forces and threshold amplitudes determined for each trial: In (**b**), the elastic force rises to a plateau that indicates the threshold required to initiate full slip. The Cattaneo–Mindlin model is plotted as a solid curve in the partial slip regime. In (**d**), linear increases in the energy dissipated over the full slip regime provide direct measurements of the average kinetic friction. The threshold amplitudes for each trial are marked with vertical black lines in (**a**) and (**c**), and the horizontal scale under (**d**) is in units of the threshold amplitude. The horizontal error bars depict the statistical fluctuations of about 5% in the measured amplitude. The variability among repeated trials in the observed stiffness and dissipation values is estimated to be about 20%, using the three trials at 100 μN

of this approach is that it eliminates the need to use continuum theories (Hertz, JKR, DMT) to model the increase in area with load, as is commonly done when no measurement is available [7]. The stiffness of a single fully stuck elastic contact is given by $k_0 = 8G^*a$, where G^* is the reduced shear modulus and a is the contact radius [42, 43]. This relationship remains valid regardless of whether adhesive forces act at the interface [43, 47]. However, plastic deformation of the gold surface by the tip is expected to produce a type of ball-in-socket geometry at the contact, possibly leading to somewhat elevated stiffness values. In using this expression, we make an informed estimate of G^* using bulk shear moduli for aluminum oxide and gold: $G^* \sim 14$ GPa. We then determine k_0 for each trial using the stiffness measured at the lowest shear amplitude, as demonstrated by the data point circled in Fig. 3a. The contact area is calculated from $A = \pi a^2 = \pi(k_0/8G^*)^2$. For the 1-mN trial in Fig. 3a, the inferred contact radius is 1.1 μm, which is a reasonable value for the load and tip size used and corresponds to an area of 3.8 μm². We present additional contact area measurements in Sect. 3.6, in the context of discussing the variation of friction and area with load.

3.5 Scaling Properties Observed Upon Varying the Load

Figure 5 shows amplitude-dependent data acquired at a variety of applied loads spanning the range of our indenter probe. Two qualitative features of these data are readily apparent from the plots of stiffness and dissipation, Fig. 5a, c: The signals increase in magnitude as the load increases to form larger contacts, and the trends versus amplitude are similar in shape for the same quantity at different loads. In fact, we find the data sets collapse to common curves when scaled to form dimensionless variables using the characteristic values F_s^*, F_k, and U_0^* determined for each trial, as with the 1-mN data set discussed earlier. Again we favor transforming the stiffness and dissipation values into quantities that can be more directly interpreted from the shape of the graph, using Eq. (3) and (2), respectively. Our results are shown in Figs. 5b, d. Figure 5b plots the normalized elastic force F_s/F_s^* versus normalized amplitude U_0/U_0^* at all loads. The common curve shows the effective elastic force rising sublinearly in good agreement with the CM microslip model until the threshold of full slip, $U_0/U_0^* = 1$, at which point the force maintains a maximum value that is roughly constant. Figure 5d displays the normalized plots of the energy
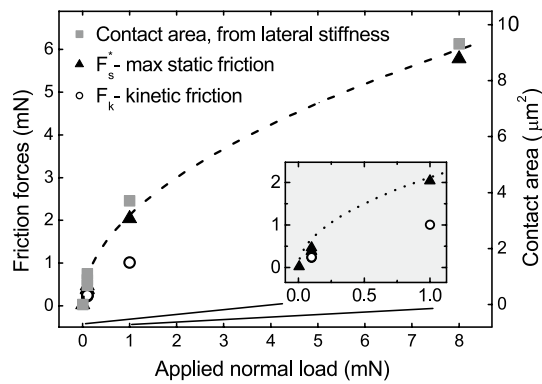
Fig. 6 Static and kinetic friction forces, and contact area, versus applied load. The inset shows the load region from 0 to 1 mN. Static friction scales with contact area over the entire range. Both quantities exhibit sublinear increases with load consistent with a square root dependence, indicated by dashed curves

loss per cycle:$\Delta W_{loss}/(4F_k U_0^*)$ versus U_0/U_0^*. The common behavior is linear growth in energy loss in the full slip state, which allows the kinetic friction to be evaluated. The threshold amplitudes are indicated with vertical bars over the data sets in Fig. 5a, c, and it is clear that larger loads lead to larger values of U_0^*. In fact, we find that F_s^*, F_k, and U_0^* all increase with load. The specific trends observed and their implications for the shear strength (friction force/area), pressure (applied load/area), and other physical results are topics of the next sections.

As a final remark, we note that data sets for ΔQ^{-1} in Fig. 5c extrapolate to nonzero values at zero amplitude, suggesting constant offsets. By inspection, the offsets show an increasing trend with load. The CM and Savkoor theories of partial slip cannot account for such offsets since they both predict that ΔQ^{-1} extrapolates to zero at the origin [32]. One possibility is that the offsets represent viscous dissipation in the contact region unrelated to slip. A similar interpretation was offered by Johnson to account for the low-amplitude behavior of macroscopic interfaces subject to oscillatory shear, on p. 231 of Johnson [43], in a discussion of experiments from the 1960s. If this damping persists at higher amplitudes it should produce quadratic growth in the energy loss, as commented earlier. The linear trends in Fig. 5d show little evidence of this, however. We propose that the observed friction at higher amplitudes is dominated by full interfacial slip.

3.6 Load Dependence of Frictional Forces and Contact Area

Variations of the frictional forces F_s^* and F_k with applied load are shown in Fig. 6. Over the range of loads from 5 μN to 8 mN, the static friction threshold F_s^* increases sublinearly, approximately as the square root of the applied

load. Meanwhile, the kinetic friction during full slip, F_k, is observed to be smaller than F_s^* by a factor of about 1.5–2 in trials conducted at both 100 μN and 1 mN, the only loads at which values for F_k could be reliably determined.[1]

The sublinear increase in F_s^* with load differs from the classical law of Amontons and Coulomb stating that friction is directly proportional to load: $F = \mu N$. Many micro- and nanoscale experimental studies have observed sublinear friction–load curves [5–7]. The frictional forces in such cases are often found to be proportional the true area of intimate contact, either by modeling the interface with contact mechanics theories or by direct observation of the contact area. In this picture, a sublinear trend in friction with load simply reflects the corresponding increase in area with load. This is described by the relation $F = \tau_0 A$, where the constant τ_0 is the interfacial shear strength. The role of the external load is limited to its influence on the area A, while τ_0 is determined by adhesive forces internal to the contact. This response has been called adhesion-controlled, or area-controlled, friction.

Our measurements of the contact area allow us to experimentally determine whether our results are accounted for within the picture of area-controlled friction. As shown in Fig. 6, we find that the increase in area with load closely follows the increase in F_s^*. This provides strong qualitative support for the area-controlled model. The next section pursues this question in further detail.

We note that the observed variability in the measured forces and areas among repeated trials at a given load, with the same tip and substrate, is commonly around 20%. In the present study, this is seen in the three trials conducted at 100 μN. We observe that the variation in force measurements is positively correlated with variation in the area, as would be expected for a system where frictional forces scale with area. Therefore, the shear strengths also seem to vary by about 20%. This variability among repeated trials dominates the experimental uncertainty in the results, since the statistical noise in measuring the quartz resonance parameters and amplitude of oscillation is comparatively small. Force measurements are also subject to 7% systematic error in the amplitude of oscillation, as mentioned earlier, while both the forces and contact areas are subject to 10% systematic error in the active area of the quartz electrode, which determines the effective mass of the crystal. The ratio of static friction to kinetic friction, however, is not subject to these systematic uncertainties due to cancelation of factors when taking the ratio.

---

[1] Kinetic friction could not be measured for the 5 μN trial, due to excessive scatter, or for the 8 mN trial, due to the large threshold amplitude to reach full slip.

Table 1 Experimental values of the applied load, pressure, static and kinetic shear strength, contact radius, and threshold amplitude

Load (mN)	p (MPa)	τ_s (MPa)	τ_k (MPa)	a (μm)	U^* (nm)
0.1	120 (30)	470 (80)	280 (70)	0.53 (0.06)	10 (1)
1.0	270	550	270	1.1	23
8.0	860	620		1.7	43

The results at a load of 0.1 mN represent averages over three separate trials, and the values in parentheses indicate the range of uncertainty among these trials

3.7 Shear Strength Measurements at Increasing Pressures

The sublinear trend in our area–load curve implies that the mean applied pressure increases with load. This is significant because it allows for a determination of whether the shear strength is strictly constant, as with $F = \tau_0 A$, or shows evidence of increasing with pressure. The more general expectation is that the shear strength is a linear function of pressure: $\tau = \tau_0 + \alpha p$, where α is the pressure coefficient [49, 50]. It is possible for either term in the linear expression for τ to dominate the behavior of the tribological system of interest. Numerous experimental and theoretical studies have shown that the relationship between shear strength and pressure can illuminate aspects of friction that remain insufficiently understood, such as the roles of adhesion, atomic roughness, larger-scale structure, and interfacial chemistry [48–54].

The shear strengths and pressures measured at each load are displayed in Table 1 along with the corresponding contact radius a and threshold amplitude U_0^*.[2] To arrive at these values, the frictional forces, F_s^* and F_k, and areas A displayed in Fig. 6 were used to compute τ_s and τ_k (where $\tau = F/A$). The pressure was found by dividing the load by the area. The values of τ_s and τ_k lie in the range of several hundred MPa, which is comparable to values reported from scanning probe experiments with a variety of rigid materials in ambient conditions [47, 48, 53–55]. We emphasize that the value for G* used to infer the contact areas is merely an informed estimate, so quantitative comparisons involving the resulting shear strengths are difficult to pursue rigorously.

Importantly, we find that both τ_s and τ_k remain relatively constant despite significant increases in pressure. The two values for τ_k are nearly identical, while the pressure more than doubles between them. The values for τ_s are seen to

rise by about 30% overall, but here the change in pressure is far larger, spanning about a sevenfold increase. This modest rise in τ_s implies that we cannot rule out a pressure coefficient α of 0.2 ± 0.2, well within the expected range [48–56]. However, the uncertainty in α is as large as the value itself. This uncertainty stems from the experimental variability in τ_s, estimated to be 20% judging from the three runs conducted at 100 μN. Therefore, it is inconclusive whether τ_s increases with pressure. It is clear, however, that within the linear model of $\tau = \tau_0 + \alpha p$, the adhesion-related term τ_0 dominates the behavior of our interfaces, while the term proportional to applied pressure, αp, plays far less of a role.

3.8 Implications for Theories of Microslip

We may use our investigation of the shear strength to evaluate the applicability of contrasting theories of microslip to our system. The Savkoor theory assumes a constant shear strength τ_0, whereas the CM theory assumes a shear strength strictly proportional to pressure, $\tau = \alpha p$ [33, 41–44]. It is interesting to note that the latter assumption corresponds to Amontons–Coulomb friction, with friction proportional to load, since $F = \tau A = \alpha p A = \alpha N$ regardless of the variation in A with N. Since our measured shear strengths are relatively insensitive to pressure (and the relations between friction and load are sublinear), our results are consistent with the assumptions adopted in the Savkoor theory. Along these lines, the study by Vlachova et al. [33] demonstrates that with sufficiently high resolution at smaller shear amplitudes, $U_0 < U_0^*$, the probe–QCM technique can distinguish further between these two theories using their contrasting predictions for the amplitude dependence of k and ΔW_{loss}. In future experiments, it should be possible to test both the assumptions and specific predictions of microslip theories within a single study.

3.9 Relationship Between the Threshold Amplitude and Contact Radius

We find that the threshold amplitude U_0^* increases approximately in proportion to the contact radius a, as shown in the two rightmost columns in Table 1. (Recall that we have used a single spherical probe and varied the load to increase the contact size.) A simple dimensional argument can account for this relationship in terms of a static friction proportional to area (constant τ_0) and a lateral stiffness proportional to a: At the threshold of full slip, the tangential elastic force is balanced with the limiting force of static friction, $k U_0^* \sim \tau_0 A$. Substituting in terms of contact radius, this becomes $(G^*a)U_0^* \sim \tau_0(\pi a^2)$. Therefore, $U_0^* \sim \tau_0(\pi a^2)/(G^*a) \sim a$. This self-consistent analysis provides additional justification for our use of the single-asperity relation $k_0 = 8G^*a$. In a previous experiment, Borovsky, Krim, Syed Asif, and Wahl demonstrated that

---

[2] At the lowest load of 0.005 mN, the shear strength for static friction was exceptionally large at 9.3 GPa. A similar low-load anomaly was observed in Ref. [47]. The effect stems from a sharp drop in lateral stiffness and inferred contact area, most likely due to the compliance of the molecular layer between the tip and sample, which may include loosely bound water or contaminants.

for a rough multi-asperity interface, the lateral stiffness of a sphere-QCM junction can be proportional to a^2 through the relation $k_0 \sim G^* a^2 / \varepsilon$, where ε is the (constant) average radius of contacting regions [23]. We can anticipate that for systems exhibiting both a multi-asperity interface and a constant shear strength, the observed thresholds U_0^* should be independent of a (and applied load), since $U_0^* \sim \tau_0 (\pi a^2) / (G^* a^2 / \varepsilon) \sim$ constant. This idea merits further investigation with probe–QCM measurements.

4 Conclusion

In summary, the combined probe–QCM technique allows for a direct measurement of forces involved in initiating and sustaining full slip motion at high-speed microscopic contacts. We have determined the frictional forces as functions of load and resolved a difference between static and kinetic friction. By quantifying the contact area via the lateral stiffness and employing a wide range of loads, we have assessed the change in mean applied pressure and investigated the extent to which the observed shear strengths depend on pressure. Finally, we have observed that the threshold amplitude to reach full slip increases about in proportion to the contact radius as the load is increased. The main advantages of the probe–QCM technique as a platform for microtribology are its sensitivity to small contacts, its high sliding speeds relevant to practical devices, and the simplicity of using the detected signals to measure both frictional forces and contact areas.

Compliance with Ethical Standards

Conflict of interest The authors declare that they have no conflict of interest.

References

1. Achanta, S., Celis, J.P.: Nanotribology of MEMS/NEMS. In: Gnecco, E., Meyer, E. (eds.) Nanoscience and Technology, pp. 631–656. Springer, Berlin (2015)
2. Mate, C.M.: Tribology on the Small Scale. Oxford University Press, New York (2008)
3. Bhushan, B.: Springer Handbook of Nanotechnology. Springer, Berlin (2010)
4. Romig, A.D., Dugger, M.T., McWhorter, P.J.: Materials issues in microelectromechanical devices: science, engineering, manufacturability and reliability. Acta Mater. **51**, 5837 (2003)
5. Stoyanov, P., Chromik, R.R.: Scaling effects on materials tribology: from macro to micro scale. Materials **10**, 550 (2017)
6. Park, J.Y., Salmeron, M.: Fundamental aspects of energy dissipation in friction. Chem. Rev. **114**, 677–711 (2014)
7. Szlufarska, I., Chandross, M., Carpick, R.W.: Recent advances in single-asperity nanotribology. J. Phys. D Appl. Phys. **41**, 123001 (2008)
8. Liu, X.Z., Ye, Z.J., Dong, Y.L., Egberts, P., Carpick, R.W., Martini, A.: Dynamics of atomic stick-slip friction examined with atomic force microscopy and atomistic simulations at overlapping speeds. Phys. Rev. Lett. **114**, 146102 (2015)
9. King, W.H.: Piezoelectric sorption detector. Anal. Chem. **36**, 1735 (1964)
10. Lu, C., Czanderna, A.W. (eds.): Applications of Piezoelectric Quartz Crystal Microbalances. Elsevier, New York (1984)
11. Johannsmann, D.: Quartz Crystal Microbalance in Soft Matter Research: Fundamentals and Modeling. Springer, Cham (2015)
12. Johannsmann, D.: Studies of contact mechanics with the QCM. In: Steinem, C., Janshoff, A. (eds.) Springer Ser Chem Se, pp. 151–170. Springer, Berlin (2007)
13. Krim, J., Widom, A.: Damping of a crystal oscillator by an adsorbed monolayer and its relation to interfacial viscosity. Phys. Rev. B **38**, 12184–12189 (1988)
14. Krim, J., Solina, D.H., Chiarello, R.: Nanotribology of a Kr Monolayer—a quartz-crystal microbalance study of atomic-scale friction. Phys. Rev. Lett. **66**, 181–184 (1991)
15. Daly, C., Krim, J.: Sliding friction of solid xenon monolayers and bilayers on Ag(111). Phys. Rev. Lett. **76**, 803–806 (1996)
16. Dybwad, G.L.: A sensitive new method for the determination of adhesive bonding between a particle and a substrate. J. Appl. Phys. **58**, 2789–2790 (1985)
17. Krim, J., Dayo, A., Daly, C.: Combined scanning tunneling microscope and quartz microbalance study of molecularly thin water layers. In: Cohen, S.H., Bray, M.T. (eds.) Atomic Force Microscopy/Scanning Tunneling Microscopy, pp. 211–215. Springer, New York (1994)
18. Sasaki, A., Katsumata, A., Iwata, F., Aoyama, H.: Scanning shearing-stress microscope. Appl. Phys. Lett. **64**, 124–125 (1994)
19. Yamada, R., Ye, S., Uosaki, K.: Novel scanning probe microscope for local elasticity measurement. Jpn. J. Appl. Phys. **2**(35), L846–L848 (1996)
20. Kim, J.M., Chang, S.M., Muramatsu, H.: Scanning localized viscoelastic image using a quartz crystal resonator combined with an atomic force microscopy. Appl. Phys. Lett. **74**, 466–468 (1999)
21. Laschitsch, A., Johannsmann, D.: High frequency tribological investigations on quartz resonator surfaces. J. Appl. Phys. **85**, 3759–3765 (1999)
22. Flanigan, C.M., Desai, M., Shull, K.R.: Contact mechanics studies with the quartz crystal microbalance. Langmuir **16**, 9825–9829 (2000)
23. Borovsky, B., Krim, J., Syed Asif, S., Wahl, K.: Measuring nanomechanical properties of dynamic contact using an indenter probe and quartz crystal microbalance. J. Appl. Phys. **90**, 6391–6396 (2001)
24. Laschitsch, A., Bailey, L.E., Tyndall, G.W., Frank, C.W., Johannsmann, D.: Frictional properties of perfluoropolyether monolayers investigated with quartz resonators. Appl. Phys. Lett. **78**, 2601–2603 (2001)
25. Dawson, B.D., Lee, S.M., Krim, J.: Tribo-induced melting transition at a sliding asperity contact. Phys. Rev. Lett. **103**, 205502 (2009)
26. Berg, S., Ruths, M., Johannsmann, D.: High-frequency measurements of interfacial friction using quartz crystal resonators integrated into a surface forces apparatus. Phys. Rev. E **65**, 026119 (2002)

27. Berg, S., Johannsmann, D.: High speed microtribology with quartz crystal resonators. Phys. Rev. Lett. **91**, 145505 (2003)

28. Borovsky, B., Booth, A., Manlove, E.: Observation of microslip dynamics at high-speed microcontacts. Appl. Phys. Lett. **91**, 114101 (2007)

29. Leopoldes, J., Jia, X.: Transverse shear oscillator investigation of boundary lubrication in weakly adhered films. Phys. Rev. Lett. **105**, 266101 (2010)

30. Leopoldes, J.L., Conrad, G., Jia, X.: Perturbation of the yield-stress rheology of polymer thin films by nonlinear shear ultrasound. Phys. Rev. E **91**, 012405 (2015)

31. Leopoldes, J., Conrad, G., Jia, X.: Onset of sliding in amorphous films triggered by high-frequency oscillatory shear. Phys. Rev. Lett. **110**, 248301 (2013)

32. Hanke, S., Petri, J., Johannsmann, D.: Partial slip in mesoscale contacts: dependence on contact size. Phys. Rev. E **88**, 032408 (2013)

33. Vlachova, J., Konig, R., Johannsmann, D.: Stiffness of sphere-plate contacts at MHz frequencies: dependence on normal load, oscillation amplitude, and ambient medium. Beilstein J. Nanotech. **6**, 845–856 (2015)

34. Inoue, D., Machida, S., Taniguchi, J., Suzuki, M., Ishikawa, M., Miura, K.: Dynamical frictional force of nanoscale sliding. Phys. Rev. B **86**, 115411 (2012)

35. Ikada, Y., Tanahara, S., Oyamada, T., Inoue, D., Machida, S., Taniguchi, J., et al.: Dynamic friction of nanoscale sliding on a C-60 deposited film. E-J. Surf. Sci. Nanotechnol. **13**, 135–138 (2015)

36. Berg, S., Ruths, M., Johannsmann, D.: Quartz crystal resonators with atomically smooth surfaces for use in contact mechanics. Rev. Sci. Instrum. **74**, 3845–3852 (2003)

37. Richter, R.P., Brisson, A.: QCM-D on mica for parallel QCM-D-AFM studies. Langmuir **20**, 4609–4613 (2004)

38. Borovsky, B., Mason, B.L., Krim, J.: Scanning tunneling microscope measurements of the amplitude of vibration of a quartz crystal oscillator. J. Appl. Phys. **88**, 4017–4021 (2000)

39. Johannsmann, D., Heim, L.O.: A simple equation predicting the amplitude of motion of quartz crystal resonators. J. Appl. Phys. **100**, 094505 (2006)

40. Mak, L.H., Knoll, M., Weiner, D., Gorschluter, A., Schirmeisen, A., Fuchs, H.: Reproducible attachment of micrometer sized particles to atomic force microscopy cantilevers. Rev. Sci. Instrum. **77**, 046104 (2006)

41. Cattaneo, C.: Sul Contatto di due Corpi Elastici: Distribuzione Locale Degli Sforzi. Rendiconti dell'Accademia Nazionale dei Lincei, Series 6, vol. 27, Part I: pp. 342–348, Part II: pp. 434–436, Part III: pp. 474–478 (1938)

42. Mindlin, R.D., Mason, W.P., Osmer, T.F., Deresiewicz, H.: Effects of an oscillating tangential force on the contact surfaces of elastic spheres. J. Appl. Mech. **18**, 331 (1951)

43. Johnson, K.L.: Contact Mechanics. Cambridge University Press, Cambridge (1987)

44. Savkoor, A.R.: Dry adhesive friction of elastomers: a study of the fundamental mechanical aspects. Ph.D. dissertation, Delft University of Technology, Netherlands (1987)

45. Mazeran, P.E., Beyaoui, M.: Initiation of sliding of an elastic contact at a nanometer scale under a scanning force microscope probe. Tribol. Lett. **30**, 1–11 (2008)

46. Konig, R., Langhoff, A., Johannsmann, D.: Steady flows above a quartz crystal resonator driven at elevated amplitude. Phys. Rev. E **89**, 043016 (2014)

47. Carpick, R.W., Ogletree, D.F., Salmeron, M.: Lateral stiffness: a new nanomechanical measurement with friction force microscopy. Appl. Phys. Lett. **70**, 1548–1550 (1997)

48. Piétrement, O., Troyon, M.: Study of the interfacial shear strength pressure dependence by modulated lateral force microscopy. Langmuir **17**, 6540–6546 (2001)

49. Bridgman, P.W.: Shearing phenomena at high pressures, particularly in inorganic compounds. Proc. Am. Acad. Arts Sci. **71**, 387–460 (1937)

50. Briscoe, B.J., Evans, D.C.B.: The shear properties of Langmuir–Blodgett layers. Proc. R. Soc. Lond. Ser. A **380**, 389–407 (1982)

51. He, G., Robbins, M.O.: Simulations of the kinetic friction due to adsorbed surface layers. Tribol. Lett. **10**, 7–14 (2001)

52. Gao, F., Furlong, O., Kotvis, P.V., Tysoe, W.T.: Pressure dependence of shear strengths of thin films on metal surfaces measured in ultrahigh vacuum. Tribol. Lett. **31**, 99–106 (2008)

53. Yang, Y., Ruths, M.: Friction of polyaromatic thiol monolayers in adhesive and nonadhesive contacts. Langmuir **25**, 12151–12159 (2009)

54. Yang, Y., Singh, J., Ruths, M.: Friction of aromatic thiol monolayers on silver: SFA and AFM studies of adhesive and non-adhesive contacts. RSC Adv. **4**, 18801–18810 (2014)

55. Schwarz, U.D., Allers, W., Gensterblum, G., Wiesendanger, R.: Low-load friction behaviour of epitaxial C_{60} monolayers under Hertzian contact. Phys. Rev. B **52**, 14976–14984 (1995)

56. Singer, I.L., Bolster, R.N., Wegand, J., Fayeulle, S., Stupp, B.C.: Hertzian stress contribution to low friction behavior of thin MoS_2 coatings. Appl. Phys. Lett. **57**, 995–997 (1990)